Journal of Power Sources 663 (2026) 238881

Contents lists available at ScienceDirect

Journal of Power Sources

journal homepage: www.elsevier.com/locate/jpowsour

Transport limitations in single-crystal NCM cathode electrodes

Roksana Jackowska [a,b,*], Nicola E. Courtier [b,c], Yongxiu Chen [a,b], Brady Planden [c], David Howey [b,c], Carmen Lopez [d], Dimitra Spathara [a,b], Emma Kendrick [a,b,*]

[a] School of Metallurgy and Materials, University of Birmingham, Elms Road, Birmingham, B15 2SE, UK
[b] Faraday Institution, Quad One, Harwell Campus, Becquerel Ave, Didcot, OX11 0RA, UK
[c] Department of Engineering Science, University of Oxford, Parks Road, Oxford, OX1 3PJ, UK
[d] National Physical Laboratory, Hampton Road, Teddington, TW11 0LW, UK

HIGHLIGHTS

- Transport and kinetic limits identified in single-crystal NCM920305 electrodes.
- Physics-based half-cell model developed and validated for optimisation.
- Model predicts 23% higher areal capacity for 70 μm thick electrodes.
- Open-source model and data provided to support community development.

GRAPHICAL ABSTRACT

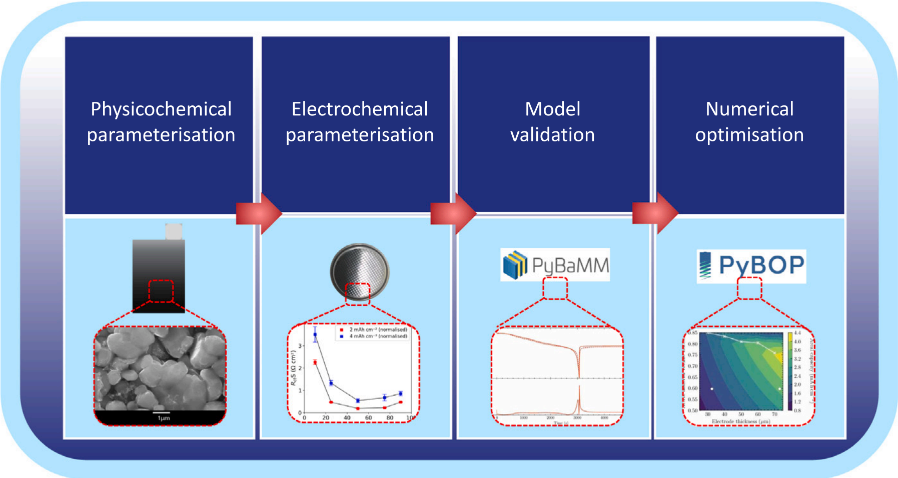

ARTICLE INFO

Dataset link: https://edata.bham.ac.uk, https://github.com/Battery-Intelligence-Lab/Jackowska-2025-JPS, https://github.com/pybamm-team/pybamm, https://github.com/pybop-team/PyBOP

Keywords:
NCM
Single crystal
Parameterisation
Battery modelling
Digital twin
Optimisation

ABSTRACT

Single-crystal $LiNi_{1-y-z}Co_zMn_yO_2$ (SC-NCM) materials are emerging as promising alternatives to polycrystalline NCMs by addressing intergranular cracking and suppressing structural degradation associated with phase transitions. However, their inherently large particle size and anisotropic morphology lead to sluggish solid-state lithium-ion transport, resulting in diffusion limitations during electrochemical cycling. To optimise SC-NCM electrodes for enhanced energy and power performance, a comprehensive understanding of how electrode level parameters, such as thickness, porosity, and active material volume fraction, influence transport properties is necessary. In this study, commercial-grade SC-NCM electrodes with areal capacities of 2 and 4 mA h cm^{-2} were examined using a suite of electrochemical and physicochemical techniques. Electronic, kinetic, and ionic transport limitations were identified in the 4 mA h cm^{-2} electrode designed for high-energy applications. Experimental data were used to parameterise and validate a physics-based half-cell model in PyBaMM, which was subsequently employed in PyBOP for numerical optimisation. By tuning key design parameters, including electrode thickness and active material volume fraction, the optimised design is predicted to deliver a 23% increase in areal 1C-discharge capacity (reaching 4.07 mAh cm^{-2}). This integrated approach combining

---

[*] Corresponding authors at: School of Metallurgy and Materials, University of Birmingham, Elms Road, Birmingham, B15 2SE, UK.
E-mail addresses: rxj139@student.bham.ac.uk (R. Jackowska), e.kendrick@bham.ac.uk (E. Kendrick).

https://doi.org/10.1016/j.jpowsour.2025.238881
Received 15 August 2025; Received in revised form 22 October 2025; Accepted 17 November 2025

modelling and experimental validation provides a pathway for optimisation of SC-NCM electrode architectures to improve energy and power metrics in lithium-ion batteries.

1. Introduction

Lithium-ion batteries (LIBs) play an increasingly prominent role in the transition towards renewable energy sources, as they are a key technology to enable both electric vehicles (EVs) and energy storage systems (ESS). With the rapid expansion of these markets, global demand for LIBs is projected to reach 2–3.5 TWh/year by 2030 [1]. Since the introduction of the layered $LiCoO_2$ (LCO) cathode chemistry in the 1980s [2], positive electrode active materials in most commercial LIBs have gradually shifted towards mixed transition metal oxides, such as polycrystalline NCM (PC-NCM) materials, driven by the need for higher specific capacity and cost reduction [3]. This shift has led to increased Ni content at the expense of Co, which, while beneficial in terms of capacity, has introduced challenges related to battery lifetime and safety [4]. These challenges stem from four key issues: cationic disorder reducing discharge capacity [5]; irreversible H2-H3 phase transitions causing intergranular cracking [6]; exposure of new electrode surfaces to side reactions and cathode electrolyte interphase (CEI) growth [7]; and electrolyte oxidation by Ni ions, leading to increased gas evolution [8]. To address these challenges, several strategies have been explored, including surface coatings [9], bulk doping [10], core–shell structures [11], and concentration gradient approaches [12]. While these have provided incremental improvements, they have not eliminated the underlying degradation mechanisms. Intergranular cracking, in particular, stands out as especially detrimental because it fragments polycrystalline secondary particles into smaller crystallites. Although this results in morphologies that superficially resemble single crystals, the electrochemical behaviour differs substantially. Crack formation exposes fresh internal surfaces to the electrolyte, promoting continuous interphase growth and parasitic reactions that consume both the electrolyte and cyclable lithium. Additionally, the loss of electrical connectivity between isolated grains reduces the active material available for cycling, directly impacting capacity retention. Cracks that propagate across the entire particle thickness can also increase mechanical stress within the electrode composite, thereby accelerating delamination from the conductive carbon/binder network.

In recent years, single-crystal NCM (SC-NCM) materials have emerged as a promising alternative to PC-NCMs, offering superior chemical and structural stability [13]. SC-NCMs are resistant to intergranular cracking, maintaining their mechanical integrity during cycling [14]. They also exhibit excellent thermal stability [15], greater volumetric energy density [16], and reduced gas generation [17]. However, this class of materials brings several new challenges that need to be addressed [18,19], particularly slow solid-state ionic transport. The large particle size and preferred crystal lattice orientation of SC-NCM particles result in longer transport pathways, slowing Li^+ diffusion along the crystal planes [20]. This slow solid-state diffusion has been linked to capacity fading during electrochemical cycling [21,22], with studies indicating that slow ionic transport, particularly at low states of charge (SOC), affects both bulk electrodes and individual particles [23]. However, current studies on this topic generally focus on the material level [17,21,22], highlighting the need for in-depth studies into how intrinsic material properties can impact performance at the electrode and cell level. Such understanding is needed for informing electrode design strategies for improved full-cell performance. SC-NCM electrode performance is ultimately limited by a combination of material-level properties and electrode-scale transport constraints. While solid-state diffusion can be improved through control of particle size and morphology, further gains can be achieved by optimising ionic and electron transport at the electrode level. This can be accomplished by tailoring electrode architecture, specifically porosity, thickness, and active material volume fraction.

The design optimisation of LIB electrodes for high energy or power density requires distinct and sometimes competing strategies, since improving one typically comes at the expense of the other [24]. High-energy density electrodes typically feature higher coat weights, lower porosity, and larger particle sizes to maximise energy storage. In contrast, high-power electrodes are designed with lower coat weights, higher porosity, and smaller particles to increase the available surface area and improve charge transfer kinetics. Empirical electrode optimisation is often time-consuming and costly, requiring extensive experimentation to achieve the desired electrode performance [25]. Numerical optimisation of a parameterised, physics-based model offers an alternative pathway to understanding and identifying optimal electrode designs [26], supporting digitalisation efforts in the electrode manufacturing processes, and reducing cost and time of LIB research and development, potentially leading to more affordable, high-performance products [27].

This study investigates two industrial-grade SC-NCM ($LiNi_{0.92}Co_{0.03}Mn_{0.05}O_2$, NCM920305) electrodes from LiFUN, with coating thicknesses of 33 μm and 73 μm, corresponding to areal capacities of 2 and 4 mA h cm^{-2}, respectively. These represent designs for high-power and high-energy applications. Physicochemical characterisation was performed using powder X-ray diffraction (PXRD), scanning electron microscopy (SEM), energy-dispersive X-ray spectroscopy (EDS), and inductively coupled plasma optical emission spectroscopy (ICP-OES), while electrochemical properties were determined via potentiostatic electrochemical impedance spectroscopy (PEIS) and galvanostatic intermittent titration technique (GITT). The extracted parameters were compiled into a standardised half-cell format compatible with `PyBaMM` [28] and used to validate model predictions against experimental rate performance. Parameter sets were then employed in `PyBOP` [29] to numerically optimise electrode thickness, porosity, and active material volume fraction. The framework identifies trade-offs between energy and power metrics and reveals that higher active material fractions can be achieved before electrolyte transport becomes rate-limiting. This integrated, physics-based approach enables targeted optimisation of SC-NCM electrodes and supports broader efforts in digital design and performance tuning. All data and code are openly available to facilitate reproducibility and community use.

2. Methodology

2.1. Physicochemical characterisation

Single-sided 2 and 4 mA h cm^{-2} capacity commercial-grade Li-ion pouch cell electrodes were sourced from Li-FUN Technology Corporation Limited (LiFUN). The electrodes were 5.2 cm long and 4.2 cm wide. The datasheet provided by the vendor included preliminary information on electrode composition, such as weight percentages of active material, binder, and conductive additive, as well as details on the active material composition, and average particle size. The electrode mass, thickness, and active material particle size were validated experimentally.

Electrode cross-sections were prepared using a Leica microtome. SEM imaging and EDS mapping were employed to examine the electrode surface and cross-sections, providing insights into morphology and elemental distributions. The electron images and EDS mapping of the NCM920305 electrodes were acquired using a Jeol7000 scanning electron microscope, operated at 20 kV acceleration voltage. The thickness of the NCM920305 electrodes and current collector was measured with an incremental length gauge (Heidenhain). To obtain the bare current-collector thickness, the single-sided NCM920305 electrode coatings were delaminated using N-Methyl-2-pyrrolidone (NMP) solvent. Electrode dimensions were measured with calipers.

Chemical analysis of the NCM920305 electrode was conducted using ICP-OES (Agilent Technologies). A 10 cm^2 electrode disc was dissolved in 10 mL of aqua regia (4:1 ratio of 38% HCl to 68% HNO_3) by heating it to 175 °C for 20 min in a microwave digestor (Anton Paar). After cooling, the solution was filtered to separate undissolved components, and the filtrate was diluted to 250 mL with distilled water. A 5 mL aliquot of this solution was further diluted to 50 mL for ICP-OES analysis. Elemental concentrations were measured in ppm and converted to atomic ratios to confirm the composition of the active material.

The crystal density of the active material was determined using PXRD measurements of the NCM920305 electrode in the 2θ range of 10-100° with a step size of 0.0149° (Proto AXRD Benchtop). Rietveld refinement of the XRD pattern was performed using the GSAS software [30]. The obtained density value was then used in the calculations of electrode porosity. The methodology for determining electrode porosity and volume fractions (active material and electrolyte) in this work follows previously reported procedures [31].

2.2. Electrochemical characterisation

The electrochemical parameterisation results are reported from an average of three individual cells or measurements, including standard deviations where possible. Electrode electronic conductivity was measured using a four-point probe (Ossila). Prior to the electronic conductivity measurement, the electrode coating was delaminated from the current collector. Delamination was achieved using a 180-degree Rheometer (Netzsch Kinexus Pro+) peel method devised in-house [32]. The delaminated samples were pressed between two glass slides before the four-point probe measurement. The pressed delaminated samples were then used to obtain electronic conductivity, with a maximum voltage of 4.3 V applied in 0.2 V voltage increments until the target current of 0.01 mA was reached. These currents were selected to minimise measurement noise, representing the maximum currents possible within the investigated voltage range. The correction factor applied during the measurement was 0.9116.

Kinetic and thermodynamic parameters were determined through electrochemical cell testing in CR2032 coin cells. The Li||NCM920305 half-cells were assembled in a dry-room (dew point of −45 °C), using 2 and 4 mA h cm^{-2} NCM920305 cathode electrodes (ϕ 14.8 mm), Celgard 2325 separator (ϕ 16 mm), lithium metal anode (ϕ 15 mm, 100 μm (±10) thickness), and two stainless steel spacers (1.5 mm total thickness) with a wave spring. The cells were prepared using 70 and 100 μL of 1M $LiPF_6$ in EC:EMC (3:7 wt. %) with 2 wt. % VC electrolyte (PiKem) for cells containing 2 and 4 mA h cm^{-2} NCM920305 electrodes, respectively. All coin cells were crimped at 1000 psi using a hydraulic coin cell crimper (TOB). Following assembly, cells underwent two formation cycles at 25 °C using a C/20 CC-CV charge and CC discharge protocol (4.2/2.5 V with C/50 cut-off current) on a BCS cycler (BioLogic). Subsequent testing was based on C-rates corresponding to the capacity stated by the manufacturer (1C equivalent to 3.44 or 6.88 mA corresponding to the 2 or 4 mA h cm^{-2} areal capacity, respectively).

The methodology for calculating lithium concentration and stoichiometry differs from previous work [25]. Prior to formation, the electrode active material is assumed to be fully lithiated, i.e., the lithium concentration equals the theoretical maximum for $LiNi_{0.92}Co_{0.03}Mn_{0.05}O_2$, given by

$$c_s^{\max} = \frac{m_{ac}}{d M \varepsilon_{ac}}, \tag{1}$$

where m_{ac} is the active material mass loading (g m^{-2}), d is the electrode coating thickness (m), M is the molar mass of the active material (g mol^{-1}), and ε_{ac} is the active material volume fraction.

During formation, a portion of lithium is irreversibly consumed via side reactions—primarily due to the formation of solid-electrolyte interphase (SEI) and cathode-electrolyte interphase (CEI) layers. Coulombic inefficiencies due to electrolyte degradation are assumed negligible. The pseudo-open-circuit voltage (pseudo-OCV) data were obtained after formation by performing a CCCV charge followed by a CC discharge at a low rate (C/20) and 25 °C. To account for formation losses, the minimum stoichiometry reached at the end of the pseudo-OCV charge is matched to that reached at the end of the initial CCCV charge (i.e., pre-formation delithiation), given by

$$x_{\min} = 1 - \frac{Q_{\text{delit.}}}{Q_{\text{th.}}}, \qquad Q_{\text{th.}} = \frac{A F d \varepsilon_{ac} c_s^{\max}}{3.6}, \tag{2}$$

where $Q_{\text{delit.}}$ is the charge capacity during initial delithiation (mA h), $Q_{\text{th.}}$ is the theoretical capacity (mA h), A is the electrode area (m^2), and F is the Faraday constant (C mol^{-1}).

The stoichiometry (x) and lithium concentration (c_{Li}^{+}) corresponding to the pseudo-OCV data are then calculated using:

$$x = x_{\min} + \frac{Q - Q_{\min}}{Q_{\text{th.}}}, \qquad c_{\text{Li}}^{+} = x c_s^{\max}, \tag{3}$$

where Q is the discharge capacity throughput (mA h) and $Q_{\min}$ is the value of Q at the end of the pseudo-OCV charge (see Supplementary Figure S8).

PEIS was performed using a VMP3 potentiostat (Bio-Logic, France) to determine the charge transfer resistance (R_{ct}) of the electrode at different states of charge (SOC). Testing was conducted at 10, 25, 50, 75, and 90% SOC, with the SOC values estimated through Coulomb counting. Before each measurement, a 180-minute rest period was allowed for the cell to reach equilibrium. The experiments were conducted in an environmental chamber at 5, 15, 25, 35, and 45 °C. Impedance spectra were recorded over a 10 mHz to 500 kHz frequency range, using a 5 mV amplitude perturbation. The spectra show several characteristic features: 2–3 overlapping semi-circles and a diffusion tail at low frequency. Data were fitted using the `ZFit` function of `EC-Lab` software using an equivalent circuit model consisting of one resistor, 3 resistor/constant phase element (R-CPE) pairs and one constant phase element in series (SI Figure S4). The charge transfer resistance R_{ct} is identified as the width of the lowest-frequency semi-circle in the PEIS spectra. Following Chen et al. [33], by linearising the Butler-Volmer equation with respect to the overpotential, the reference exchange current density (j_0) at a given operating point (i.e. stoichiometry and temperature) can be calculated from the charge transfer resistance by

$$j_0(x, T) = \frac{RT}{F S R_{ct}(x, T)}, \tag{4}$$

where R is the ideal gas constant (J K^{-1} mol^{-1}), T is the temperature (K), and S is the active surface area (m^2).

The series resistance and double-layer capacitance were also obtained from the fitting of the PEIS data using the equivalent circuit model (SI Figure S4). In a Nyquist plot, the series resistance corresponds to the point where the curve intersects the real axis at the highest frequency. For the model (Section 2.3), a *lumped* series resistance, which accounts for unmodelled high-frequency behaviour, is required. The lumped resistance is therefore the sum of the series resistance and the resistance values for each of the two highest-frequency semi-circles. The double-layer capacitance was obtained directly from the PEIS fitting as the equivalent capacitance associated with the lowest-frequency R-CPE element. The fitted capacitance values (in F) were then normalised by the electrochemically active surface area (S) of each electrode to yield values in F m^{-2}, which are reported in Table 2.

GITT was used to measure the apparent diffusion coefficient (D_{Li^+}) of both NCM920305 electrodes at different temperatures. C/10 current pulses were applied for 10 min, followed by a 3 h rest period to reach an equilibrium open circuit voltage (OCV).

Electrode tortuosity was assessed using a previously reported symmetrical cell impedance methodology [34,35]. CR2032 coin cells were assembled in a dry-room (dew point of −45 °C) with a glass fibre separator (ϕ 16 mm) sandwiched between two cathode electrode discs (ϕ 14.8 mm) and 100 μL of 100 mM tetrabutylammonium perchlorate salt ($TBAClO_4$) in EC: DMC (1:1 wt. %) electrolyte prepared in-house. After an 8 h rest in open-circuit conditions, the frequency range of 10 mHz to 500 kHz with a 5 mV amplitude was applied for testing. Electrode ionic resistance (R_{ion}) was calculated from the x-axis intercepts of two lines of best fit (x_1, x_2; see SI Figure S7), and then the tortuosity factor (τ) was calculated as follows,

$$R_{\mathrm{ion}} = 3(x_2 - x_1), \qquad \tau = \frac{R_{\mathrm{ion}} \kappa A \varepsilon}{2d}, \tag{5}$$

where κ is the electrolyte ionic conductivity ($\mathrm{S\,m^{-1}}$) and ε is the electrode porosity. A conductivity value of $0.29\,\mathrm{S\,m^{-1}}$ was obtained from interpolating previously reported results on $TBAClO_4$ salts in EC: DMC (1:1 wt. %) electrolytes by Landesfeind et al. [34].

Rate performance testing was performed for lithiation in Li||NCM920305 half-cells at 25 °C. For the discharge (lithiation) rate test, a fixed constant current (CC) of C/2 or C/5 (for 2 and $4\,\mathrm{mA\,h\,cm^{-2}}$ electrodes, respectively) was used to charge until 4.2 V vs. Li/Li^+. Then, CC discharge (lithiation) rates of nC (where n = 0.1, 0.2, 0.5, 1, 2) were used sequentially to discharge to 2.5 V vs. Li/Li^+. A rest of 30 min was used after each discharge cycle.

2.3. Modelling and simulation details

For validation and design optimisation, the Doyle-Fuller-Newman (DFN) model is used to capture the electrolyte dynamics as well as the de/lithiation behaviour. This work uses the open-source software `PyBaMM` (version `25.6`) and `PyBOP` (version `25.6`) [28,29,36]. The DFN model in `PyBaMM` [28,37] is adapted into a half-cell model by neglecting the negative-electrode dynamics and setting the positive electrode as the working electrode. The model is constructed in `PyBaMM` by setting the `‘‘working electrode’’` option to `‘‘positive’’`. The lithium-metal counter electrode is modelled using an exchange current density for an asymmetric Butler-Volmer reaction between lithium metal and the electrolyte [38] given by

$$j_0^{\mathrm{Li}} = m_{\mathrm{ref}} c_{\mathrm{Li}}^{0.7} c_{\mathrm{e}}^{0.3}, \tag{6}$$

where m_{ref} is the reaction rate parameter ($\mathrm{A\,m^{-2}\,(mol\,m^{-3})}$) and c_{Li} is the pure metal lithium concentration ($\mathrm{mol\,m^{-3}}$).

In the positive electrode, the reference exchange current density is modelled assuming a symmetric reaction (assuming a charge transfer coefficient of 0.5 [37]) via

$$j_0(c_{\mathrm{e}}, c_s, T) = k(T)\sqrt{c_{\mathrm{e}} c_s \left(c_{\mathrm{s}}^{\max} - c_s\right)}, \tag{7}$$

where k is the reaction rate ($\mathrm{A\,m^{-2}\,(m^3\,mol^{-1})^{1.5}}$), c_{e} is the electrolyte concentration ($\mathrm{mol\,m^{-3}}$), and c_s is the particle surface concentration ($\mathrm{mol\,m^{-3}}$). Under the small voltage perturbations applied during PEIS, it can be assumed that c_{e} remains at its initial, bulk value $c_{\mathrm{e},0}$, and that the particle surface concentration is approximated by the average concentration $x c_s^{\max}$, where x is the mean stoichiometry at a given SOC. This simplification allows for a more computationally efficient fitting of the exchange current density while maintaining the essential SOC dependence:

$$j_0(x, T) = k(T)\, c_{\mathrm{s}}^{\max} \sqrt{c_{\mathrm{e},0}\, x\,(1 - x)}. \tag{8}$$

This equation is used to fit the reaction rate at a given temperature to the values of the reference exchange current density obtained via (4) from PEIS measured at five different values of SOC (x).

The dependence of the reaction rate on temperature is modelled using an Arrhenius relation as follows.

$$k(T) = k_{\mathrm{ref}} \exp\left[\frac{E_{\mathrm{ct}}}{R}\left(\frac{1}{T_{\mathrm{ref}}} - \frac{1}{T}\right)\right], \tag{9}$$

where $k_{\mathrm{ref}} = k(T_{\mathrm{ref}})$ is the reaction rate constant, T_{ref} is the reference temperature (K), and E_{ct} is the activation energy ($\mathrm{J\,mol^{-1}}$). The activation energy is fitted to the values of the reaction rate obtained from (8) at five different temperatures.

To model each GITT pulse, a spherical diffusion model with a stoichiometry-dependent diffusion timescale (τ_D) and a lumped resistance (R_s) is used. The convention is that a positive current ($I > 0$) corresponds to lithiation (discharging) of the half-cell:

$$\frac{\partial c}{\partial t} = \frac{1}{r^2}\frac{\partial}{\partial r}\left(\frac{r^2}{\tau_D(c)}\frac{\partial c}{\partial r}\right) \qquad \text{in } 0 < r < 1, \tag{10}$$

$$\text{with } \left.\frac{1}{\tau_D(c)}\frac{\partial c}{\partial r}\right|_{r=0} = 0, \qquad \left.\frac{1}{\tau_D(c)}\frac{\partial c}{\partial r}\right|_{r=1} = \frac{I(t)}{3Q_{\mathrm{th.}}}, \tag{11}$$

$$V(t) = \mathrm{OCV}\left(c|_{r=1}\right) - R_s\left(c|_{r=1}\right) I(t) \tag{12}$$

Here, $Q_{\mathrm{th.}} = F\varepsilon_{\mathrm{ac}} d A c_s^{\max}$ is the theoretical capacity (A s). The two parameters (τ_D and R_s) are fitted simultaneously to each pulse and subsequent relaxation using `SciPy minimize` within `PyBOP`, taking care to weight the unevenly-spaced data points by the proportion of time spent closest to each point.

The compiled NCM920305 `PyBaMM` half-cell parameters were validated by comparing the simulation results with experimental rate capability data from both NCM920305 electrodes. Design optimisation was performed using `PyBOP` [29] and its implementation of the `SciPy` differential evolution algorithm, using a maximum of 25 iterations, or `SciPy minimize` with up to 250 iterations.

3. Results and discussion

3.1. Physicochemical parameterisation

The structures and compositions of the two NCM920305 electrodes were analysed using ICP-OES, PXRD, and SEM-EDX. SEM analysis of the electrode surface revealed small cuboid particles in both electrodes, measuring between 1-5 μm, with distinctive steps or ridges visible at certain angles (Figs. 1c and f). EDS mapping confirmed the uniform distribution of Ni, Co, and Mn elements throughout the electrodes (Figs. 1d and g). PXRD analysis of the $2\,\mathrm{mA\,h\,cm^{-2}}$ electrode identified a preferred orientation along the 003 plane, indicating crystal growth along the c-axis (Fig. 1a). This orientation likely contributes to the observed ridged surfaces and supports identification of the particles as single crystals. Additionally, PXRD Rietveld refinement showed that lithium predominantly occupies its designated site, with minimal transition metal-lithium mixing. Results from Rietveld refinement including chi-squared, wRp, Rp, lattice parameters, bond lengths, and preferred orientation ratios are summarised in SI Table S1.

Atomic ratios calculated from ICP-OES analysis of the $2\,\mathrm{mA\,h\,cm^{-2}}$ electrode were 86.1: 93.6: 2.8: 4.7 for Li: Ni: Co: Mn elements, closely matching the expected composition for the pristine $LiNi_{0.92}Co_{0.03}Mn_{0.05}O_2$ material. The residue from microwave digestion was further analysed to identify the binder and conductive additive in the electrode. SEM-EDS analysis of the washed and dried residue revealed the presence of C and F elements (SI Figure S1). These elements, which are resistant to aqua regia digestion [39], were attributed to PVDF binder and carbon-black conductive additive.

Based on these findings, the solid volume fraction of the NCM920305 electrodes was calculated as the ratio between the measured electrode coating density and the theoretical solid material density. A theoretical solid material density of $4.48\,\mathrm{g\,cm^{-3}}$ was determined, assuming the electrode composition ratios specified by the vendor and considering electrode components including PVDF binder, carbon black conductive additive, and $LiNi_{0.92}Co_{0.03}Mn_{0.05}O_2$ active material with a density of $4.796\,\mathrm{g\,cm^{-3}}$ as obtained from Rietveld refinement (Fig. 1a). Using this density, the porosity of the NCM920305 electrodes was calculated to be 29% and 33% for the 2 and $4\,\mathrm{mA\,h\,cm^{-2}}$ electrodes, respectively. Cross-sectional images of the electrodes

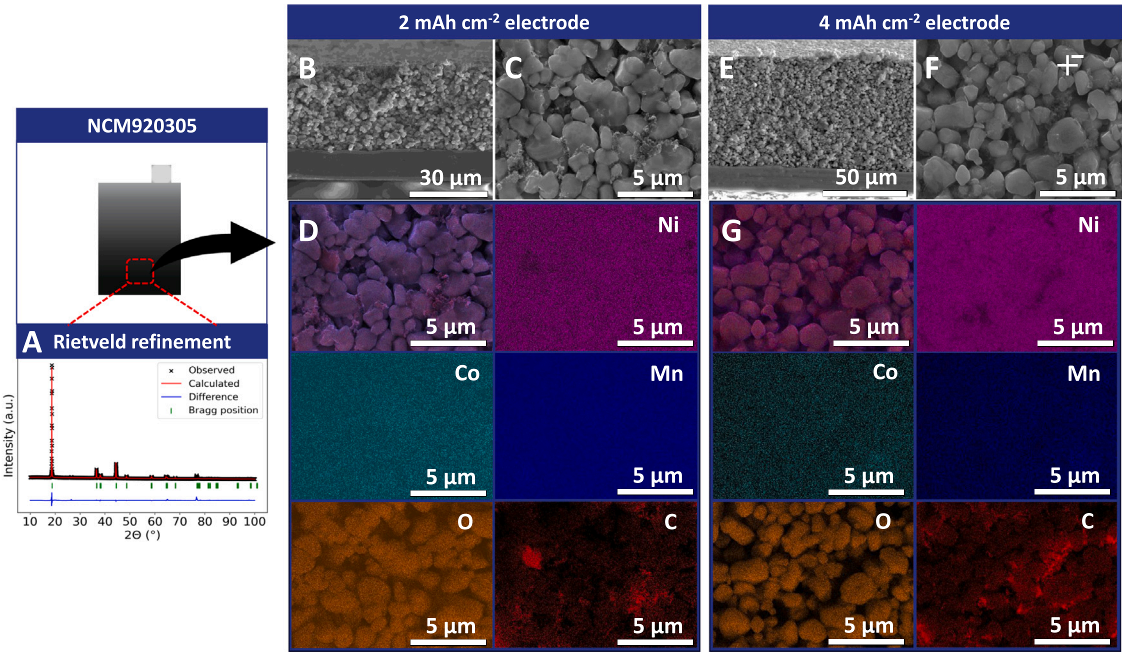

Fig. 1. Analysis of NCM920305 single-layer pouch cell electrodes: observed (black 'x' symbols), calculated (red line), and difference (blue line) profiles from Rietveld refinement of PXRD data for the 2 mA h cm^{-2} electrode, together with Bragg positions attributed to the NCM811 phase (green ticks) (a); cross-section SEM image of the 2 mA h cm^{-2} electrode (b); electrode surface SEM image showing cuboid-shaped particles in 2 mA h cm^{-2} electrode (c) and its corresponding EDS mapping of Ni (purple), Co (green), Mn (blue), O (orange), and C (red) elements (d); cross-section SEM image of the 4 mA h cm^{-2} electrode (e); electrode surface SEM image showing cuboid-shaped particles in 4 mA h cm^{-2} electrode (f) and its corresponding EDS mapping of Ni (purple), Co (green), Mn (blue), O (orange), and C (red) elements (g).

Table 1
Summary of parameters determined, and derived, from physicochemical characterisation of the two NCM920305 electrodes.

Parameter (Symbol)	Unit	Value for NCM920305 electrodes		Source/Definition
Nominal areal capacity	mA h cm^{-2}	2	4	Datasheet
Active material	–	$LiNi_{0.92}Co_{0.03}Mn_{0.05}O_2$		Datasheet
Current collector thickness (d_{cc})	m	12×10^{-6}		Length gauge
Total electrode thickness	m	44.5×10^{-6}	85.0×10^{-6}	Length gauge
Electrode diameter	m	0.0148		Calipers
Particle radius (r)	m	1.88×10^{-6}		Datasheet
Electrode coating weight (w_{ct})	g	0.018 56	0.039 46	Electrode delamination/balance
Active material loading (l_{ac})	wt %	95.5		Supplier datasheet
Active material density (ρ_{ac})	g m^{-3}	4.796×10^6		Rietveld refinement
Combined carbon-binder density (ρ_{cb})	g m^{-3}	1.86×10^6		Supplier information
Electrolyte density (ρ_{el})	g m^{-3}	1.203×10^6		Supplier information
Electrode coating thickness (d)	m	32.5×10^{-6}	73×10^{-6}	Total electrode thickness - d_{cc}
Electrode area (A)	m^2	1.72×10^{-4}		π(Electrode diameter/2)^2
Representative electrode width and height	m	0.0131		$\sqrt{A}$
Solid material density	g m^{-3}	4.48×10^6		$[l_{ac}/\rho_{ac} + (1 - l_{ac})/\rho_{cb}]^{-1}$
Active material weight	g	0.017 72	0.037 68	$l_{ac} w_{ct}$
Active material mass loading (m_{ac})	g m^{-2}	103	219	$l_{ac} w_{ct}/A$
Electrode mass loading	g m^{-2}	108	229	w_{ct}/A
Electrode coating density (ρ_{ct})	g m^{-3}	3.32×10^6	3.14×10^6	$w_{ct}/(dA)$
Electrolyte volume fraction (or porosity, ε)	–	0.259	0.299	1 - ρ_{ct}/Solid material density
Active material volume fraction (ε_{ac})	–	0.661	0.625	$l_{ac}\rho_{ct}/\rho_{ac}$
Combined carbon-binder volume fraction	–	0.080	0.076	$1 - \varepsilon - \varepsilon_{ac}$
Active surface area (S)	m^2	0.0059	0.0125	$3\varepsilon_{ac} dA/r$, from [33] eqn. (10)
Active surface area per unit volume	m^{-1}	1.05×10^6	0.997×10^6	$3\varepsilon_{ac}/r$

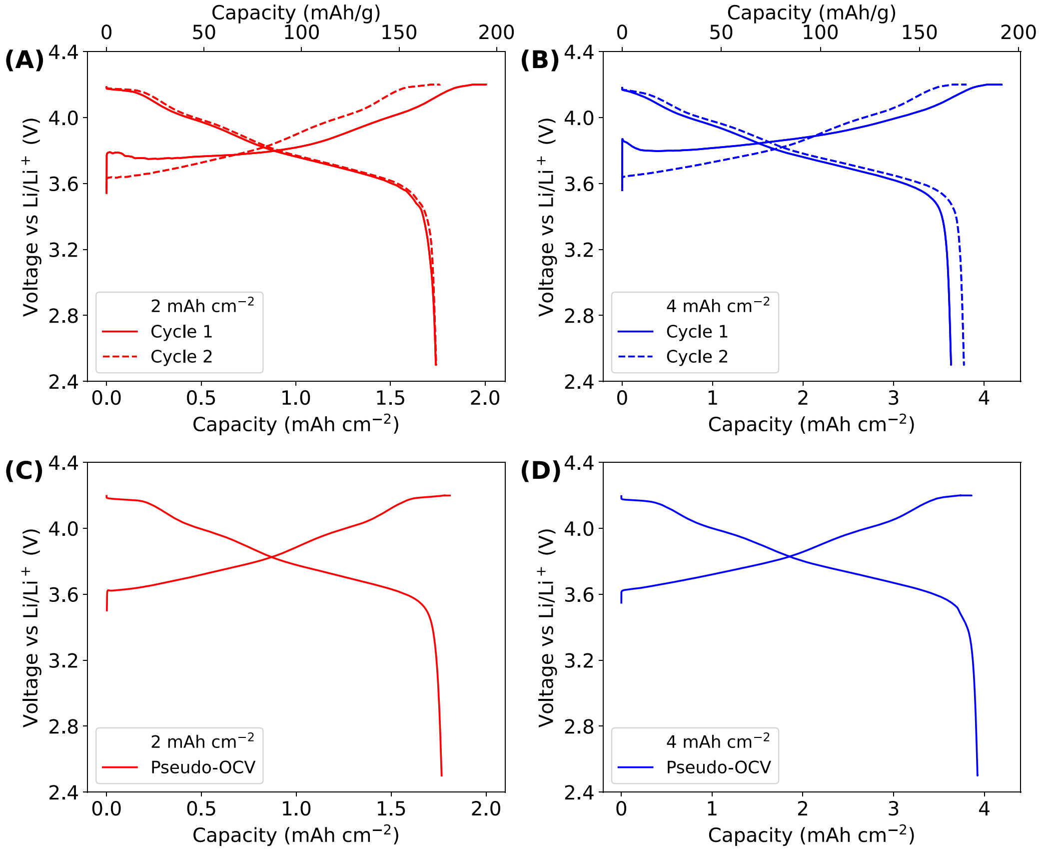

Fig. 2. Formation data for Li||NCM920305 half-cells with different coating thickness: 2 mA h cm^{-2} (a) and 4 mA h cm^{-2} (b), together with the pseudo-OCV data measured after formation for 2 mA h cm^{-2} (c) and 4 mA h cm^{-2} (d) electrodes.

showed a consistent microstructure and particle distribution throughout (Figs. 1b and e).

The parameters determined and derived from the physicochemical characterisation of the 2 and 4 mA h cm^{-2} electrodes are summarised in Table 1, detailing the source or definition of each parameter. The parameters obtained in this study were used to create `PyBaMM` half-cell parameter files for each electrode, for model validation and electrode optimisation.

3.2. Electrochemical parameterisation

3.2.1. Formation, lithium concentration and stoichiometry

Figs. 2a and b show the formation results for both electrodes. The average practical capacities for the NCM920305 electrodes, achieved during the first formation cycle, were 2.02 mA h cm^{-2} (±0.07) and 4.16 mA h cm^{-2} (±0.16), which closely matched the datasheet specifications. While the theoretical specific capacity for the $LiNi_{0.92}Co_{0.03}Mn_{0.05}O_2$ active material is 275 mA h g^{-1}, the measured specific capacities were 196 mA h g^{-1} (±7) and 190 mA h g^{-1} (±7) for active material within the 2 and 4 mA h cm^{-2} electrodes, respectively.

During formation, the average first and second cycle efficiencies were comparable: 86.8% (±0.4) and 99.4% (±0.03) for the 2 mA h cm^{-2} electrode, and 87.1% (±0.8) and 99.5% (±0.1) the 4 mA h cm^{-2} electrode, respectively. The losses from the first formation cycle are ascribed to lithium inventory loss from active material to form SEI/CEI interphase layers, as losses associated with electrolyte decomposition are relatively small in comparison [25].

The as-formed cells were used in pseudo-OCV, PEIS, GITT, and rate capability measurements. Figs. 2c and d show the pseudo-OCV data for both electrodes, used in calculations of lithium concentration and stoichiometry according to Eq. (3).

The maximum lithium concentration, as well as all other parameters identified from the electrochemical characterisation, are summarised at the end of this section in Table 2.

3.2.2. Electronic transport

The electronic conductivity of the electrodes was characterised using 4-point probe conductivity measurement on delaminated electrode coatings. Fig. 3f shows that the in-plane conductivity of the 2 mA h cm^{-2} electrode closely matches that of the 4 mA h cm^{-2} electrode. This similarity is expected, given that both electrodes were fabricated with identical formulations, including the same conductive additive content, differing only in electrode coating thickness.

3.2.3. Intercalation reaction kinetics

PEIS was conducted to investigate the charge-transfer resistance (R_{ct}) in Li||NCM920305 half-cells across various states of charge (SOC): 10, 25, 50, 75, and 90%, and temperatures spanning 5, 15, 25, 35, and 45 °C, thereby elucidating temperature-dependent trends in the reaction kinetics of SC-NCM electrodes. The Nyquist plots of the PEIS spectra between 10 and 90% SOC, measured at 25 °C for both NCM920305 electrodes, are shown in Fig. 4. The Nyquist plots of the PEIS spectra summarising measurement results across all SOC points and temperatures are depicted in SI Figure S2 and S3 for the 2 mA h cm^{-2} and 4 mA h cm^{-2} electrodes, respectively. The fit (black lines on the plots) was performed using an equivalent circuit model (SI Figure S4), providing an excellent fit across all SOC and temperature conditions.

All R_{ct} values exhibited a decreasing 'L'-shaped trend with increasing SOC, consistent with previous studies [31]. Notably, the R_{ct} values demonstrate only marginal variations between the two electrodes (SI Figure S5). To elucidate the charge-transfer properties of both electrodes across different temperatures, the R_{ct} values have been normalised with respect to the material active surface area (S)

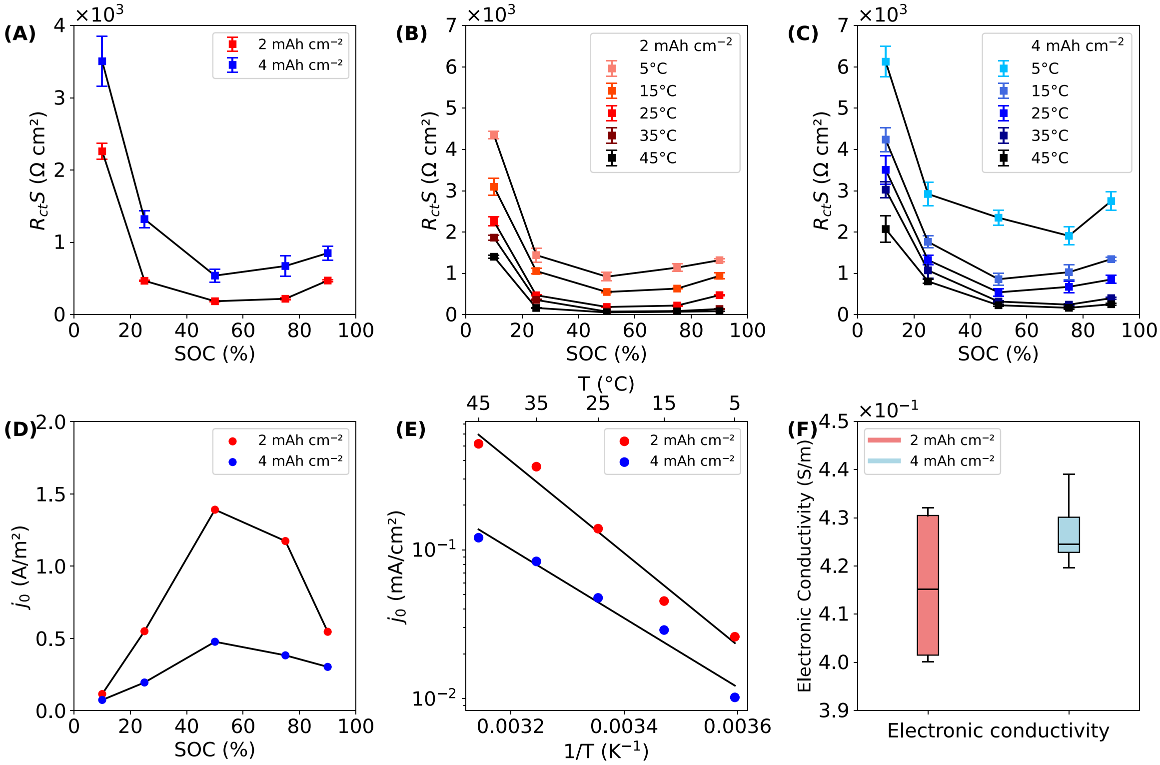

Fig. 3. Charge transfer resistivity ($R_{ct}S$) identified from PEIS on Li||NCM920305 half-cells for 2 mA h cm^{-2} and 4 mA h cm^{-2} electrodes measured at 25 °C (a); 2 mA h cm^{-2} electrode measured at 5, 15, 25, 35, and 45 °C (b); and 4 mA h cm^{-2} electrode measured at 5, 15, 25, 35, and 45 °C (c). Derived values for reference exchange current density (d) for 2 mA h cm^{-2} and 4 mA h cm^{-2} electrodes at 25 °C. Arrhenius representation of temperature dependence of j_0 for 2 mA h cm^{-2} and 4 mA h cm^{-2} electrodes, based on PEIS results at 50% SOC, with linear fits (in black) (e). Electronic conductivity results for NCM920305 electrodes (f).

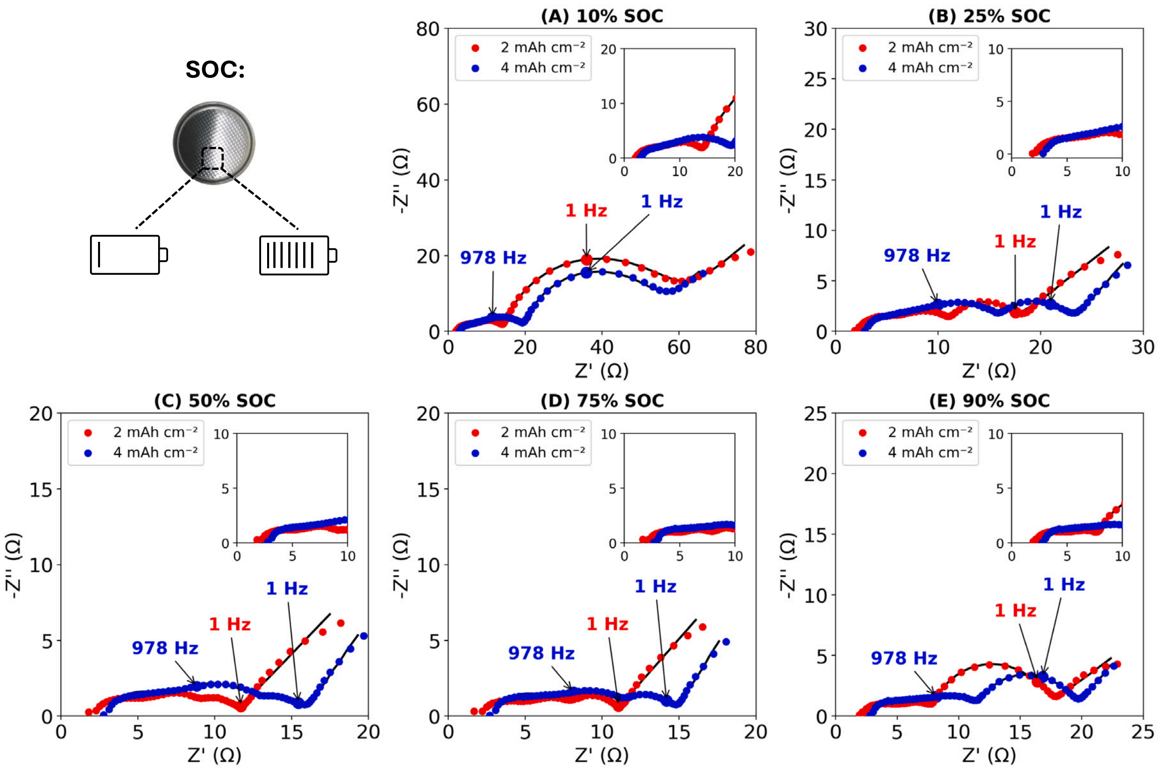

Fig. 4. The Nyquist plots of the PEIS for the 2 mA h cm^{-2} (in red) and 4 mA h cm^{-2} (in blue) electrodes, measured at 10% (a), 25% (b), 50% (c), 75% (d), and 90% SOC (e) at 25 °C. The fit (black lines on the plots) was performed using an equivalent circuit shown in SI Figure S4. Magnifications of each Nyquist plot depict the high-frequency region and the series resistance of both electrodes (the x-axis intercept).

of each electrode (total surface area of the active material particles contained within a 1.72 cm^{-2} electrode area). It should be noted that S was calculated by assuming spherical shape of NCM920305 particles, and not taking into account the preferred orientation of the particles, nor the anisotropic diffusion within particles. Fig. 3a depicts the normalised R_{ct} values at 25 °C for both electrodes, whilst Figs. 3b and c show the temperature dependence of the normalised values for the 2 $\mathrm{mA\,h\,cm^{-2}}$ and 4 $\mathrm{mA\,h\,cm^{-2}}$ electrodes, respectively. Considering the electrode thickness difference, the 4 $\mathrm{mA\,h\,cm^{-2}}$ electrode exhibits slightly reduced charge transfer efficiency. The highest R_{ct} values were recorded at the lowest measured SOC of 10% for both electrodes across all temperatures. The values remain high at 25% SOC across all temperatures, indicating that the rate of the charge transfer process remains slow at low SOC. At 50% SOC, R_{ct} values reached their minimum for both electrodes across all temperatures, indicating an accelerated intercalation of solvated Li^+ ions in the electrolyte into the active material.

The double-layer specific capacitance and resistance values obtained from PEIS are reported in Table 2. The difference between the series resistances of the 2 and 4 $\mathrm{mA\,h\,cm^{-2}}$ electrodes stems from the increased amount of electrolyte used in the 4 $\mathrm{mA\,h\,cm^{-2}}$ Li||NCM920305 half-cell, variation in the thickness of the Li foil, and the x-axis intercept not being sharply defined in the collected spectra.

To further elucidate the kinetics of Li^+ (de)intercalation in NCM920305 electrodes, changes in the exchange current density (j_0), reaction rate constant (k_{ref}) and activation energy (E_{ct}) were characterised, as defined in Eqs. (8)–(9). The j_0 values are displayed in 3d, derived from R_{ct} values obtained from PEIS at 25 °C. Both electrodes displayed similarly low j_0 values at 10% SOC. However, at 50% SOC, j_0 significantly increased to 1.390 $\mathrm{A\,m^{-2}}$ for the 2 $\mathrm{mA\,h\,cm^{-2}}$ electrode, whereas the 4 $\mathrm{mA\,h\,cm^{-2}}$ electrode only reached 0.476 $\mathrm{A\,m^{-2}}$. This represents an almost 200% increase in j_0 for the thinner electrode relative to its higher-loading counterpart (Fig. 3d). These results are in good agreement with the j_0 values obtained by modelling the reference exchange current density under the assumption of a symmetric reaction (SI Figure S12a and b), as described in (8). The modelled values are summarised in Table 2 and used for model validation and optimisation in this study.

Activation energy (E_{ct}) was determined by fitting the slope of the Arrhenius plot. The temperature dependence of experimentally derived j_0 values for both electrodes is depicted in Fig. 3e, with all j_0 values derived from PEIS measurements at 50% SOC. The Arrhenius plot indicates that j_0 increases with temperature for both electrodes, demonstrating temperature-dependent interfacial kinetics. It should be noted that the plotted E_{ct} values correspond specifically to 50% SOC and represent apparent activation energies that encompass multiple interfacial processes, including Li^+ desolvation, charge transfer, and near-surface migration [40–42]. Different values would be expected at other SOCs due to variations in electrode thermodynamics and interfacial conditions. The 2 $\mathrm{mA\,h\,cm^{-2}}$ electrode exhibits higher j_0 values across all temperatures, indicating more favourable charge transfer kinetics. Interestingly, this electrode also shows a higher E_{ct} (56,410 J/mol) compared to the 4 $\mathrm{mA\,h\,cm^{-2}}$ electrode (46,040 J/mol). This suggests that although the 2 $\mathrm{mA\,h\,cm^{-2}}$ electrode benefits from improved interfacial kinetics and its performance is more sensitive to temperature variations, with pronounced improvement at elevated temperatures likely due to reduced electrolyte mass transport limitations. The modelled E_{ct} values are again in good agreement with experimentally derived values, and are used in Table 2 at the end of this section.

3.2.4. *Solid-state ionic transport*

To determine apparent lithium diffusivity, GITT was conducted on Li||NCM920305 half-cells. The modelled GITT profiles at 25 °C use particle radius of 1.88 μm. The results, including the root mean square error (RMSE) between the model-predicted voltage and the pulse data, are shown in SI Figure S10. The diffusivity and resistance estimates with RMSE below 5 mV were interpolated to generate functions of stoichiometry. The interpolated functions were used to simulate each GITT experiment using the spherical diffusion model, and the results are plotted against the experimental data in SI Figure S11.

The GITT fitting results for the 2 and 4 $\mathrm{mA\,h\,cm^{-2}}$ electrodes are shown in Figs. 5a and b, respectively. The results show that the apparent solid-state diffusion of both electrodes is similar, which is expected since both electrodes contain $\mathrm{LiNi_{0.92}Co_{0.03}Mn_{0.05}O_2}$ active material. Applying low current (C/10) during the GITT measurement eliminates any impact from electrolyte ion mass transport. Minimal differences in the apparent diffusion coefficient values between charge and discharge were observed, consistent with previous studies on SC-NCM materials [43]. The apparent diffusion coefficient reached its highest values near 50% SOC for both electrodes (Figs. 5a and b), with an upward trend in values at temperatures above 25 °C for the 2 $\mathrm{mA\,h\,cm^{-2}}$ electrode, as pictured in SI Figure S6. In contrast, a decreasing trend was observed at temperatures below this threshold.

However, despite a 180-minute relaxation period after each pulse in GITT measurement, it was observed that above 3.9 V versus $\mathrm{Li/Li^+}$, the steady-state potential was never fully reached for both electrodes as the voltage gradually decreased. One possible explanation for this is oxygen release occurring from cation mixing at the particle surface and gradual structure collapse, as previously studied elsewhere [44]. This phenomenon impacts the determination of apparent diffusion coefficients in some voltage ranges because the assumption of equilibrium underlying GITT analysis is no longer strictly valid. Therefore, the values reported above 3.9 V versus $\mathrm{Li/Li^+}$ should be considered lower-bound estimates of the true diffusion coefficient, as part of the relaxation signal includes parasitic processes rather than solely Li^+ transport. This indicates that in the high-voltage region, the extracted coefficients are affected by electrode degradation phenomena and may not reflect the intrinsic Li^+ transport properties of NCM920305.

For assessing the tortuosity factor of the NCM920305 electrode, PEIS was performed in a symmetric cell configuration, where two NCM920305 electrodes of identical thickness and capacity were placed on either side of a separator within a coin cell, and an ion-blocking electrolyte was used to restrict insertion of mobile ions. The tortuosity factor was calculated to be 3.43 and 3.88 for the 2 and 4 $\mathrm{mA\,h\,cm^{-2}}$ electrodes, respectively, using (5). SI Figure S7 illustrates how the x-axis intercepts were determined for both electrodes, and the derived R_{ion} values are listed in Table 2. These relatively high tortuosity values are likely due to the active material shape and small average particle size, which is only 3.76 μm in diameter. Tortuosity critically affects ion transport and rate performance in Li-ion cells by increasing Li^+ diffusion paths through porous electrodes. Higher tortuosity reduces ion transfer rates, as reflected in the lower rate capability of the 4 $\mathrm{mA\,h\,cm^{-2}}$ electrode (Fig. 6b), and may also impair long-term cycling stability due to stress-induced electrode degradation [45]. Interestingly, the tortuosity does not increase significantly with increasing coat weight, indicating that further electrode design optimisation is possible.

Rate capability measurements for Li||NCM920305 half-cells at 25 °C are shown in Figs. 6a and b for the 2 and 4 $\mathrm{mA\,h\,cm^{-2}}$ electrodes, respectively. The 2 $\mathrm{mA\,h\,cm^{-2}}$ electrode demonstrated excellent high-rate performance, retaining 98% and 96% of its C/10 capacity at 1C and 2C (1.71 and 1.68 $\mathrm{mA\,h\,cm^{-2}}$). In contrast, the 4 $\mathrm{mA\,h\,cm^{-2}}$ electrode showed reduced retention of 90% and 32% (3.31 and 1.90 $\mathrm{mA\,h\,cm^{-2}}$) at the same rates, consistent with transport limitations in thicker electrodes. The improved performance of the thinner electrode is attributed to lower tortuosity and reduced thickness, which enhance Li^+ transport. Limitations imposed by the Li metal counter electrode—especially at high current densities may contribute to the poor 2C performance of the 4 $\mathrm{mA\,h\,cm^{-2}}$ cell, where current reaches 8 $\mathrm{mA\,cm^{-2}}$ [31,46,47]. At such rates, the Li-metal surface undergoes rapid dendrite formation, uneven stripping and plating, and accelerated electrolyte depletion,

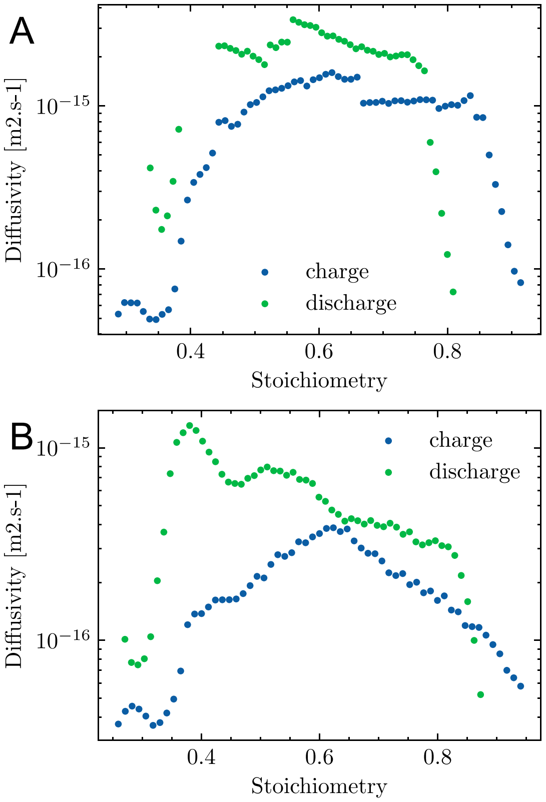

Fig. 5. The diffusivity estimates calculated as $D = R^2/\tau_D$ for the 2 mA h cm^{-2} (a) and 4 mA h cm^{-2} (b) electrodes, where R is the particle radius of 1.88 µm.

leading to unstable interphase growth and increased interfacial resistance. These processes consume electrolyte and active lithium, leading to large overpotentials on the Li side that artificially limit the measured capacity and rate capability of the 4 mAh cm^{-2} NCM920305 electrode in a half-cell configuration. As a result, the intrinsic kinetic performance of this electrode cannot be fully isolated under these conditions. A more precise assessment could be obtained through full-cell studies (although these can have their own limitations due to the size of the negative electrode), or ideally, using a three-electrode setup, where a stable reference and a larger counter electrode enable accurate monitoring of the positive electrode potential under various operating conditions. To avoid artefacts from counter electrode limitations, model validation excluded the 2C rate data.

3.3. Model validation

The determined and derived physicochemical and electrochemical parameters for 2 and 4 mA h cm^{-2} NCM920305 electrodes are summarised in Tables 1–2. Based on the parameters collected in this work, `PyBaMM` half-cell parameter files were created for each electrode and made available on GitHub. The half-cell parameter files for NCM920305 electrodes use previously published Li metal parameters from Xu et al. [38], and 1 M LiPF$_6$ in EC:EMC (3:7) electrolyte parameters from Landesfeind et al. [48]. The information on separator thickness and porosity came from the supplier datasheet, whilst the Bruggeman coefficient for electrolytes was also used by Xu et al. [38]. The completed `PyBaMM` half-cell parameter files are discussed and validated in this section.

To validate the parameters obtained from the experimental methods, model simulations were compared against discharge data from rate capability experiments, as shown in Fig. 7. A detailed breakdown of the model validation at each C-rate is provided in SI Figure S13. Model validation was performed by adjusting the apparent diffusion coefficient for each C-rate to achieve good agreement between experiments and simulations, as required for previous validations of the DFN model versus experimental data [33,49]. Building on prior model validations, the apparent diffusion coefficient function is used during validation to account for changes in diffusivity with increasing stoichiometry. However, it was still observed that the model required different diffusion coefficient parameters at each C-rate. The variation in the diffusivity scaling factor and root mean squared error (RMSE) for the validation at each C-rate are shown in SI Figure S14. This is expected if the model overlooks specific physics, such as particle size distribution, or if there are inaccuracies in calculated parameters, for example, in determining the electrochemically active area of SC-NCM electrodes, or if fixed parameter values are used during validation. The need to adjust the apparent diffusion coefficient at each C-rate likely reflects physical heterogeneities not captured by the assumption of uniform, spherical particles in the DFN model. In reality, the SC-NCM electrode exhibits a distribution of particle sizes (Fig. 1c and f), meaning smaller particles lithiate and delithiate more rapidly, leading to local variations in Li$^+$ concentration and overpotential. Moreover, preferred crystallographic orientation along the (003) axis and the intrinsically anisotropic Li$^+$ diffusion in layered oxides further contribute to spatially heterogeneous transport, as Li$^+$ mobility across basal planes is limited. These effects become increasingly pronounced under high-rate conditions, resulting in apparent diffusivity variations with C-rate and limiting the full generalisability of the optimised model parameters.

For design optimisation, a generalised parameter set was compiled based on the values identified for the two different electrode thicknesses (SI Table S2). Using a generalised parameter set is necessary because it provides a starting point for the optimisation, constrained by the boundary conditions defined by 2 and 4 mA h cm^{-2} electrodes. The open-circuit voltage, diffusion coefficient, and maximum lithium concentration of the 2 mA h cm^{-2} electrode were used. For every other parameter, either a mean value or a fitted function was used in the generalised parameter values. The fitted functional parameters are listed in Table 3. The corresponding results for 2 and 4 mA h cm^{-2} electrodes are also plotted for comparison against the optimised results.

3.4. Electrode design optimisation

Electrode design must be tailored to the intended application, whether prioritising high gravimetric and volumetric energy density at low rates or high power delivery at elevated rates. At the pack level, optimisation targets focus on maximising usable energy and power (Wh kg^{-1}, Wh L^{-1}, W kg^{-1}, W L^{-1}). In contrast, at the electrode level - particularly in half-cell studies - the focus shifts to transport and kinetic limitations within the coating, with parameters such as thickness, porosity, and active material loading tuned to balance energy- and power-oriented performance. Areal metrics are particularly suitable here, as they avoid assumptions about full-cell component masses or volumes.

Although particle size was not explicitly investigated in this study, it would be expected to have a profound effect on the simulation results. With a distribution of particle sizes in the SC-NCM electrode, the time to fully (de)lithiate each particle will differ. Smaller particles have shorter Li$^+$ diffusion lengths and can therefore fully lithiate more quickly, with the high surface area leading to faster apparent kinetics. However, the large surface area also increases interfacial reactivity, which can exacerbate first-cycle irreversible capacity loss through side reactions at the electrolyte–electrode interface. In contrast, larger particles have longer diffusion paths, leading to steeper concentration gradients, increased overpotential, and longer complete (de)lithiation under high-rate conditions, due to a lower surface area to particle volume ratio. Additionally, the preferred crystallographic orientation along the (003) axis imposes anisotropic Li$^+$ mobility, as diffusion across the basal planes is comparatively sluggish. These combined

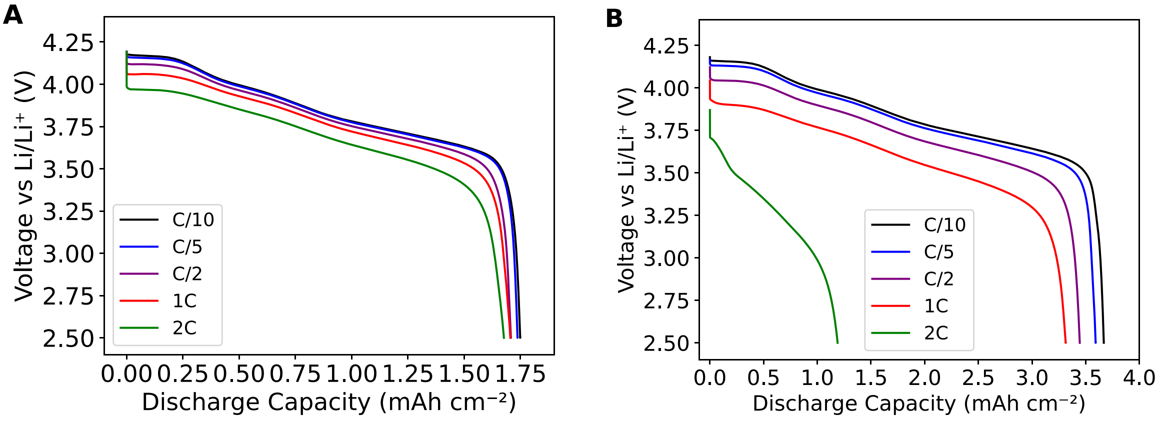

Fig. 6. Rate capability of the NCM920305||Li half-cells, showing variable rate CC discharge (lithiation), measured at 25 °C for the 2 mA h cm^{-2} (a) and 4 mA h cm^{-2} electrode (b).

Table 2
Summary of parameters determined, and derived, from electrochemical characterisation of the two NCM920305 electrodes.

Parameter (Symbol)	Unit	Value for NCM920305 electrodes 2 mA h cm^{-2}	 4 mA h cm^{-2}	Source/Definition
Open-circuit voltage (OCV)	V	Function, Fig. 2a	Function, Fig. 2b	Pseudo-OCV after formation
Maximum lithium conc. (c_s^{max})	mol m^{-3}	49 225	49 225	Eq. (1)
		55 370	48 980	Fit to C/10 discharge
Electronic conductivity	S m^{-1}	0.416	0.427	4-point probe
Charge transfer resistivity ($R_{ct}S$)	Ω m^2	Function, Fig. 3a	Function, Fig. 3a	Normalised ECM fit to PEIS
		0.0194	0.0564	Value at 50% SOC, 25 °C
Double-layer specific capacitance	F m^{-2}	6.86×10^{-3}	3.74×10^{-3}	Normalised ECM fit to PEIS
Series resistance	Ω	2.5	3.4	PEIS x-axis intercept
High-frequency resistance	Ω	4.20	5.30	ECM fit to PEIS
Lumped resistance	Ω	6.70	8.70	Sum of PEIS resistances
		22.4	23.4	Fit to 1C discharge
Solid-phase diffusivity (D_{Li}^{+})	m^2 s^{-1}	Function, Fig. 5a	Function, Fig. 5b	GITT
		1.81×10^{-16}	5.52×10^{-16}	Value at 50% SOC, 25 °C
Diffusivity scaling factor	–	8.58	2.46	Fit to 1C discharge
Ionic resistance (R_{ion})	Ω	17.25	37.98	PEIS on symmetric cells
Electrolyte conductivity (κ)	S m^{-1}	0.29		Interpolated from [34]
Initial electrolyte conc. ($c_{e,0}$)	mol m^{-3}	1000		Supplier datasheet
Reference temperature (T_{ref})	K	298.15		Unless otherwise stated
Lithium metal reaction rate (m_{ref})	A m^{-2} (mol m^{-3})	$3.5 \times 10^{-8} F$		[38]
Pure metal lithium conc. (c_{Li})	mol m^{-3}	$1/(1.3 \times 10^{-5})$		[38]
Ref. exch. current density (j_0)	A m^{-2}	Function, Fig. 3e	Function, Fig. 3e	Eq. (4), at 25 °C
		1.328	0.456	Value at 50% SOC, 25 °C
Reaction rate constant (k_{ref})	A m^{-2} (m^3 mol^{-1})$^{1.5}$	1.037×10^{-6}	0.436×10^{-6}	Fit to Eqs. (8)–(9)
Activation energy (E_{ct})	J mol^{-1}	56 410	46 040	Fit to Eqs. (8)–(9)
Tortuosity factor (τ)	–	3.43	3.88	Eq. (5)
Bruggeman exponent	–	1.90	2.12	$1 - \log(\tau)/\log(\varepsilon)$ [33,34]

effects influence both the apparent diffusivity and reaction uniformity within the electrode. Currently, the model lacks a mechanistic link between increased surface area and first-cycle loss, which means that the negative impact of particle size reduction on practical capacity is not captured. Future model extensions incorporating particle size distributions and anisotropic solid-state diffusion would provide a more physically representative description of transport and rate limitations.

In this work, electrode-specific properties are investigated in `PyBOP` using areal 1C-discharge capacity (mAh cm^{-2}) and areal fixed-rate discharge energy (mWh cm^{-2}) as primary optimisation targets. These targets directly capture the balance between electrode architecture parameters that govern performance in high-energy and high-power applications. For these 1C-discharge targets, the C-rate must be estimated as part of the optimisation.

To illustrate the sensitivity of specific capacity (mAh g^{-1}) to electrode design, an additional optimisation was performed using an estimated negative-electrode mass, with results shown in SI Figure S15. This example highlights the trade-off between increasing electrode thickness—which raises areal capacity—and the corresponding decrease in specific capacity once counter-electrode mass is considered.

The aim of the optimisation is to quantify how controllable material parameters influence cell performance. In `PyBOP` the active material volume fraction and electrode thickness are varied to assess their combined effect on capacity and rate capability. Increasing either parameter raises the theoretical capacity but also reduces porosity, which exacerbates electrolyte transport limitations and accelerates the onset of power-limited behaviour at higher rates. These competing effects are quantified using the validated parameter sets from this work, as shown in Fig. 8.

3.4.1. *Areal discharge capacity*

The first target selected for design optimisation is the areal 1C-discharge capacity (mAh cm^{-2}), defined as

$$Q_{\text{ar.}} = \frac{1}{3.6A} \int_{t=0}^{t=t_f} I(t)\,\mathrm{d}t, \tag{13}$$

where A is the cell area (cm^2); $I(t)$ is the current (A) required to discharge the half-cell from 4.2 to 2.5 V followed by a 30-minute rest; and t_f is the time taken (s). The areal 1C-discharge capacity is an

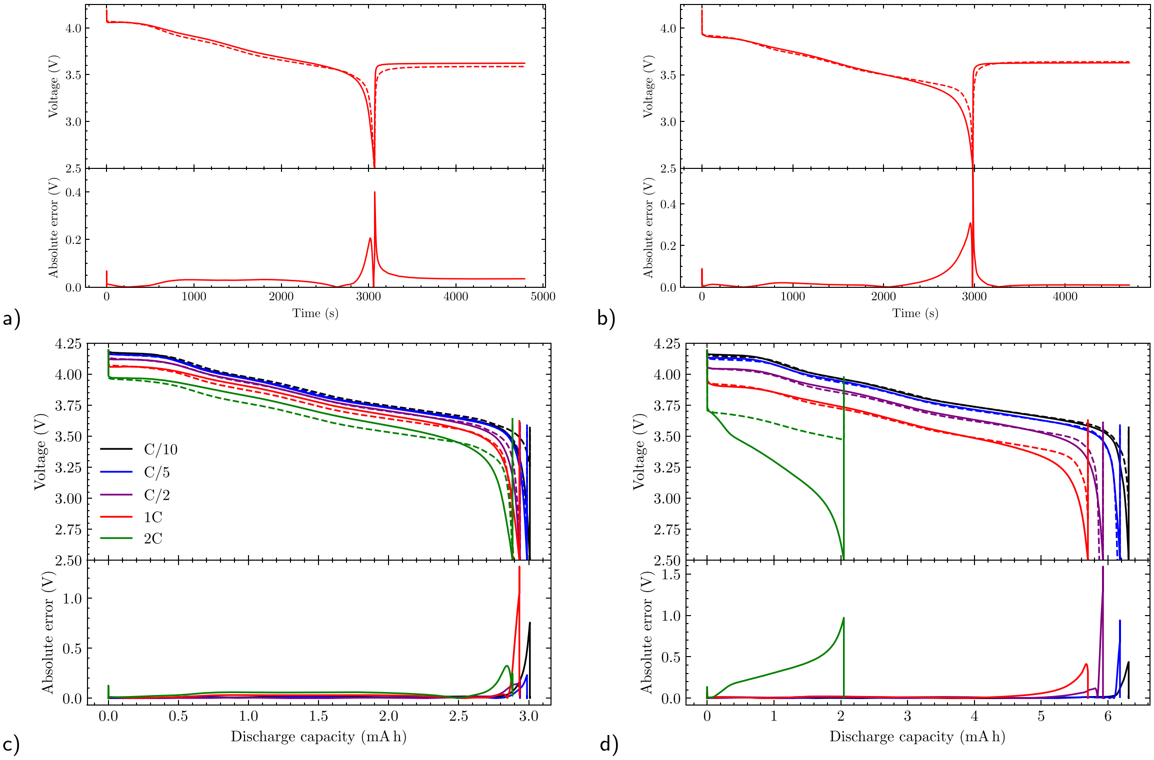

Fig. 7. Validation of model predictions (dashed lines) against experimental CC discharge-rest data (solid lines) for the 2 mA h cm^{-2} electrode (a, c) and 4 mA h cm^{-2} (b, d) using the DFN parameter values from Tables 1 and 2. Only the apparent diffusion coefficient is required to vary with C-rate to reproduce the rate-performance (SI Figure S14).

appropriate target for high-energy applications, as it favours thicker cells with a higher accessible capacity.

3.4.2. Areal discharge energy

The second target for design optimisation is the areal fixed-rate discharge energy (mWh cm^{-2}), defined as

$$E_{\mathrm{ar.}} = \frac{1}{3.6A}\int_{t=0}^{t=t_{\mathrm{f}}} I(t)V(t)\,\mathrm{d}t, \tag{14}$$

where A is the cell area (cm^2); $I(t)$ is the current (A) corresponding to a 5 mA discharge for 30 min or until 2.5 V, followed by a 30 min rest; $V(t)$ is the output voltage (V); and t_{f} is the time taken (s). As expected, the areal fixed-rate energy also favours thicker cells. In this case, the cost function is

$$L\left(\epsilon_{\mathrm{ac}}, d\right) = E_{\mathrm{ar.}}. \tag{15}$$

3.4.3. Nominal capacity

The nominal capacity (which defines the C-rate) for different battery designs cannot be defined a priori, as the value specified in the validated `PyBaMM` files was measured at a C/20 rate rather than at 1C. To account for this, the nominal capacity ($Q_{\mathrm{nom.}}$) is included as an additional optimisation parameter along with a penalty term in the cost function equal to the number of seconds a simulation is short of the target length of the experiment, which is 1.5 h. The cost function (L) to maximise is therefore defined as

$$L\left(\epsilon_{\mathrm{ac}}, Q_{\mathrm{nom.}}, d\right) = Q_{\mathrm{ar.}} + 5400 - t_{\mathrm{f}}. \tag{16}$$

The optimisation parameters are bounded by minimum and maximum values, which are given in Table 3. Also listed are the set of other model parameters which are assumed to directly depend on one of the optimisation parameters, namely the lumped resistance, reaction rate constant, Bruggeman exponent, double-layer capacitance, the diffusivity factor identified from the 1C rate capability test, and the porosity. A full set of model parameters is given together in the SI Table S2.

3.4.4. Optimisation results

The optimisation results shown in Fig. 8 explore the impact of the electrode thickness and active material volume fraction on the theoretical rate-performance of SC-NCM electrodes. The cost landscape in Fig. 8a illustrates how the areal 1C-discharge capacity varies with the two geometric optimisation parameters. A higher electrode thickness increases the electrode capacity, however, as expected, there is a trade-off between the active material volume fraction and the porosity (for any given electrode thickness), which can be seen from the drop in discharge capacity at very high active material volume fractions (low porosity). Through joint numerical optimisation of the three optimisation parameters, it is found that a theoretical increase in the areal 1C-discharge capacity from 3.31 on the validated 4 mA h cm^{-2} parameter set to 4.07 mA h cm^{-2} for a 70 μm-thick electrode may be achieved.

The optimisation results reveal that, for example, an improved, 70 μm-thick NCM electrode would have an optimal porosity of just 16.4%. Such a low value in comparison to the identified porosity values suggests that the model of electrolyte transport may be too simplistic to fully capture the importance of a high porosity. While electrodes with very low porosity, such as 16%, can be fabricated, particularly in PVDF binder-containing versions, through 'over-calendaring' at higher temperatures. Reduction in porosity will increase the gravimetric and volumetric energy densities of the cells. However, their practical use may be limited due to various challenges. Lithium transport through solid-state diffusion in the active material is significantly lower than in liquid electrolyte within the pores of the electrode. This means that such electrodes may only operate at very low current densities. Additionally, at 16% porosity, some pores could remain inaccessible to the electrolyte due to the percolation theory. Achieving this would require the pore size to be very small and uniformly dispersed throughout the electrode. However, there may still be substantial lithium mass transport limitations to the surface of the active material particles throughout the electrode, leading to high overpotentials and possible

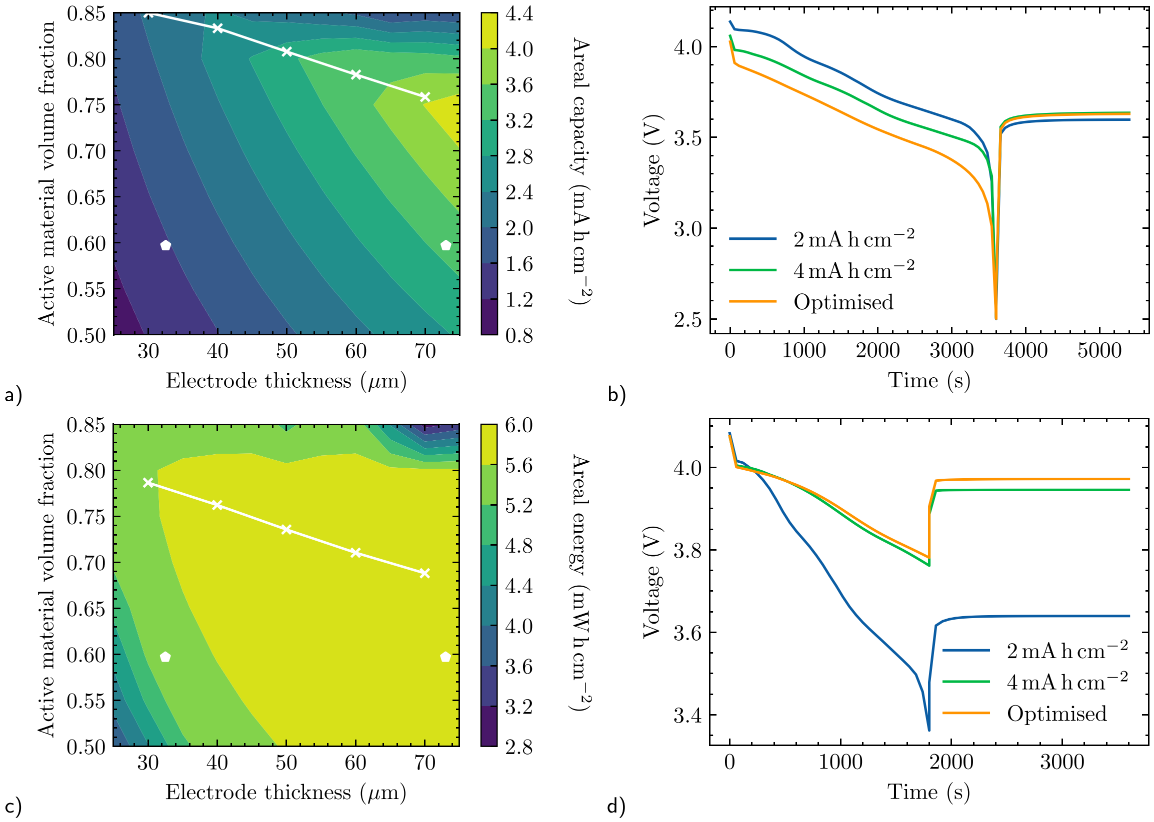

Fig. 8. Electrode optimisation results from `PyBOP`: (a) Cost landscape showing areal 1C-discharge capacity as a function of two of the three optimisation parameters: active material volume fraction and electrode thickness. The third optimisation parameter is nominal capacity, which controls discharge rate; optimal discharge rate is 1C for the corresponding geometric parameters. The cell parameters validated in Fig. 7 are depicted using white pentagons (with predicted $Q_{\mathrm{ar.}}$ of 1.57 and 3.31 mA h cm^{-2} for the 2 and 4 mA h cm^{-2} electrodes, respectively). Optimised active material volume fraction for theoretical 40, 50, 60 and 70 µm-thick electrodes are indicated by the connected white crosses. (b) Simulations of 1C discharge from 4.2 to 2.5 V, followed by 30-minute rest, for three different parameter sets: the two validated parameter sets and the 70 µm-thick optimised parameter set in Table 3. (c) Cost landscape showing areal fixed-rate discharge energy as a function of active material volume fraction and electrode thickness, with white markers as in (a). (d) Simulations of 5 mA discharge for 30 min or until 2.5 V, followed by 30-minute rest, for validated and 70 µm-thick optimised parameter sets.

poor long-term performance. Fig. 8b shows the very similar discharge profiles of the validated and the optimised 70 µm-thick electrode designs. The corresponding difference in areal capacity is due to the 1C-discharge rate rising from 5.69 to 7.00 mA.

The cost landscape in Fig. 8c shows the impact of the two geometric optimisation parameters on the areal fixed-rate discharge energy. As before, mass transport through the electrolyte provides an upper limit on the active material volume fraction for a given electrode thickness. Overall, the areal energy shows a much lower sensitivity to the electrode thickness, shown by the large area of the parameter space that predicts a value of 5.6 mW h cm^{-2} or higher (yellow area). Only a slight increase in the areal discharge energy from 5.52 mW h cm^{-2} for the validated 2 mA h cm^{-2} parameter set to 5.77 mW h cm^{-2} for a 70 µm-thick electrode is predicted. In this case, the optimised porosity is 23.4%. Fig. 8d shows simulated discharge profiles which underpin the calculation of the areal fixed-rate discharge energy.

4. Conclusions

In this study, two single-crystal NCM920305 electrodes of varying thickness and capacity were characterised to evaluate the influence of electrode architecture on transport and interfacial kinetics. Although both electrodes exhibited similar in-plane conductivity, reflecting their identical formulation and conductive additive content, substantial differences in transport behaviour were observed. The thicker 4 mA h cm^{-2} electrode was found to suffer from electrolyte mass transport limitations, attributed to its increased tortuosity (3.88 versus 3.43 for the thinner 2 mA h cm^{-2} electrode), hindering lithium-ion diffusion through the porous structure. These effects, combined with increased charge-transfer resistance and reduced exchange current density, contributed to diminished rate capability and kinetic performance in the 4 mA h cm^{-2} electrode.

A parameterised half-cell model was developed using `PyBaMM` and validated against experimental rate capability data. Numerical optimisation of selected parameters, performed using `PyBOP` framework, further explored the interplay of key electrode design aspects, active material volume fraction and electrode thickness, and their impact on specific 1C-discharge capacity. The optimisation predicted a potential increase of 23% in the areal 1C-discharge capacity, reaching 4.07 mA h cm^{-2} for a 70 µm-thick electrode with a higher active material volume fraction and reduced porosity.

The integration of experimental data with modelling and optimisation tools has demonstrated a viable approach to guiding electrode design. The presented methodology provides a foundation for accelerating the design of SC-NCM electrodes and addressing the trade-offs between energy and power performance in LIBs. The optimisation results underscore the importance of electrode design in achieving high-energy-density applications, highlighting that carefully chosen parameters can minimise resistive losses and maintain favourable kinetic profiles in thicker electrode designs. By making the parameter sets and simulation files openly available, the authors support transparency and accessibility of the results. The methodology developed in this work may be extended to a broad range of chemistries, including layered oxides with different compositions or emerging battery chemistries,

Table 3
Summary of optimisation parameters and functional dependence of other model parameters on optimisation parameters. Areal 1C-discharge capacity and areal fixed-rate discharge energy are the design targets.

Optimisation parameter	Unit	Range	Optimised value
Electrode coating thickness (d)	m	[40, 50, 60, 70] $\times 10^{-6}$	70×10^{-6}
Active material volume fraction (ε_{ac})	–	0.5 – 0.85	0.758
Nominal capacity	mA h	2.5 – 7.5	7.00
Areal 1C-discharge capacity	$\mathrm{mA\,h\,cm^{-2}}$	–	4.07
Areal fixed-rate discharge energy	$\mathrm{mW\,h\,cm^{-2}}$	–	5.77
Function parameter		**Function used in the optimisation**	
Lumped resistance	Ohm	$21.5 + 2.60\times10^{5}d$	
Reaction rate constant (k_{ref})	$\mathrm{A\,m^{-2}\,(m^3mol^{-1})^{1.5}}$	$3.27\times10^{-11}/d$	
Bruggeman exponent	–	$1.72 + 5432d$	
Double-layer specific capacitance	$\mathrm{F\,m^{-2}}$	$2.48\times10^{-7}/d$	
Diffusivity factor at 1C	–	$1 + (7.42\times10^{-5}/d)^2$	
Electrolyte volume fraction (or porosity, ε)	–	$1 - \varepsilon_{ac} - 0.078$	

and leveraged to investigate advanced electrode designs. This approach offers a powerful tool for accelerating electrode optimisation and bridging the gap between materials discovery and cell-level performance engineering.

CRediT authorship contribution statement

Roksana Jackowska: Writing – review & editing, Writing – original draft, Visualization, Methodology, Investigation, Formal analysis, Data curation, Conceptualization. **Nicola E. Courtier:** Writing – review & editing, Writing – original draft, Validation, Methodology, Investigation, Formal analysis, Data curation. **Yongxiu Chen:** Writing – review & editing, Methodology, Investigation, Formal analysis. **Brady Planden:** Writing – original draft, Methodology, Investigation, Formal analysis. **David Howey:** Writing – review & editing, Supervision, Resources, Project administration. **Carmen Lopez:** Supervision. **Dimitra Spathara:** Writing – review & editing, Investigation. **Emma Kendrick:** Writing – review & editing, Supervision, Resources, Project administration, Methodology, Funding acquisition, Conceptualization.

Declaration of competing interest

The authors declare that they have no known competing financial interests or personal relationships that could have appeared to influence the work reported in this paper.

Acknowledgements

This work was supported by the Multi-Scale Modelling project, funded by the Faraday Institution (grant numbers FITG042 and FIRG084). The authors would like to thank Dr. Robert Timms for his invaluable knowledge and guidance on model validation and creating `PyBaMM` half-cell files, Dr. Elizabeth Driscoll for her support in running the ICP-OES setup, and Dr. Dominika Gastol for suggestions and guidance during the preparation of this manuscript.

Appendix A. Supplementary data

Supplementary material related to this article can be found online at https://doi.org/10.1016/j.jpowsour.2025.238881.

Data availability

Experimental data are available on the UBIRA eData repository https://edata.bham.ac.uk. `PyBaMM` half-cell parameter files for the 2 and 4 $\mathrm{mA\,h\,cm^{-2}}$ electrodes and the scripts used for this work are available at https://github.com/Battery-Intelligence-Lab/Jackowska-2025-JPS. `PyBaMM` simulation code is available at https://github.com/pybamm-team/pybamm. `PyBOP` parameterisation and optimisation code is available at: https://github.com/pybop-team/PyBOP.

References

[1] J. Frith, M. Lacey, U. Ulissi, A non-academic perspective on the future of lithium-based batteries, Nat. Commun. 14 (1) (2023) 1–17, http://dx.doi.org/10.1038/s41467-023-35933-2.

[2] K. Mizushima, P. Jones, P. Wiseman, J. Goodenough, Li_xCoO_2 ($0 < x < 1$): A new cathode material for batteries of high energy density, Solid State Ionics 3-4 (1981) 171–174, http://dx.doi.org/10.1016/0167-2738(81)90077-1.

[3] A. Manthiram, A reflection on lithium-ion battery cathode chemistry, Nat. Commun. 11 (1) (2020) 1550, http://dx.doi.org/10.1038/s41467-020-15355-0.

[4] R. Sim, A. Manthiram, Factors influencing gas evolution from high-nickel layered oxide cathodes in lithium-based batteries, Adv. Energy Mater. 14 (8) (2024) 1–13, http://dx.doi.org/10.1002/aenm.202303985.

[5] M. Jiang, D. Danilov, R.-A. Eichel, P. Notten, A review of degradation mechanisms and recent achievements for Ni-rich cathode-based Li-ion batteries, Adv. Energy Mater. 11 (48) (2021) 2021, http://dx.doi.org/10.1002/aenm.202103005.

[6] S. Jamil, G. Wang, L. Yang, X. Xie, S. Cao, H. Liu, B. Chang, X. Wang, Suppressing H2-H3 phase transition in high Ni-low Co layered oxide cathode material by dual modification, J. Mater. Chem. A 8 (40) (2020) 21306–21316, http://dx.doi.org/10.1039/D0TA07965K.

[7] T. Kim, Voltage-dependent formation of cathode-electrolyte interphase with independent metallic layer in $LiNi_{0.8}Mn_{0.1}Co_{0.1}O_2$ cathode for high-energy density lithium-ion batteries, Mater. Today Sustain. 21 (2023) 100326, http://dx.doi.org/10.1016/j.mtsust.2023.100326.

[8] B. Rowden, N. Garcia-Araez, A review of gas evolution in lithium ion batteries, Energy Rep. 6 (2020) 10–18, http://dx.doi.org/10.1016/j.egyr.2020.02.022.

[9] G. Kaur, B. Gates, Review—Surface coatings for cathodes in lithium ion batteries: From crystal structures to electrochemical performance, J. Electrochem. Soc. 169 (4) (2022) 043504, http://dx.doi.org/10.1149/1945-7111/ac60f3.

[10] W. Yan, S. Yang, Y. Huang, Y. Yang, G. Yuan, A review on doping/coating of nickel-rich cathode materials for lithium-ion batteries, J. Alloys Compd. 819 (2020) 153048, http://dx.doi.org/10.1016/j.jallcom.2019.153048.

[11] P. Hou, H. Zhang, Z. Zi, L. Zhang, X. Xu, Core-shell and concentration-gradient cathodes prepared via co-precipitation reaction for advanced lithium-ion batteries, J. Mater. Chem. A 5 (9) (2017) 4254–4279, http://dx.doi.org/10.1039/c6ta10297b.

[12] Y.-K. Sun, Z. Chen, H.-J. Noh, D.-J. Lee, H.-G. Jung, Y. Ren, S. Wang, C. Yoon, S.-T. Myung, K. Amine, Nanostructured high-energy cathode materials for advanced lithium batteries, Nat. Mater. 11 (11) (2012) 942–947, http://dx.doi.org/10.1038/nmat3435.

[13] K. Homlamai, N. Anansuksawat, N. Joraleechanchai, P. Chiochan, T. Sangsanit, W. Tejangkura, T. Maihom, J. Limtrakul, M. Sawangphruk, Microcracking of Ni-rich layered oxide does not occur at single crystal primary particles even abused at 4.7 V, Chem. Commun. 58 (81) (2022) 11382–11385, http://dx.doi.org/10.1039/d2cc03977j.

[14] Y. Lu, T. Zhu, E. Mcshane, B. Mccloskey, G. Chen, Single-crystal $LiNi_xMn_yCo_{1-x-y}O_2$ cathodes for extreme fast charging, Small 18 (12) (2022) 2105833, http://dx.doi.org/10.1002/smll.202105833.

[15] X. Kong, Y. Zhang, J. Li, H. Yang, P. Dai, J. Zeng, J. Zhao, Single-crystal structure helps enhance the thermal performance of Ni-rich layered cathode materials for lithium-ion batteries, Chem. Eng. J. 434 (2022) 134638, http://dx.doi.org/10.1016/j.cej.2022.134638.

[16] B. You, Z. Wang, F. Shen, Y. Chang, W. Peng, X. Li, H. Guo, Q. Hu, C. Deng, S. Yang, G. Yan, J. Wang, Research progress of single-crystal nickel-rich cathode materials for lithium ion batteries, Small Methods 5 (8) (2021) 2021, http://dx.doi.org/10.1002/smtd.202100234.

[17] J. Hu, L. Li, Y. Bi, J. Tao, J. Lochala, D. Liu, B. Wu, X. Cao, S. Chae, C. Wang, J. Xiao, Locking oxygen in lattice: A quantifiable comparison of gas generation in polycrystalline and single crystal Ni-rich cathodes, Energy Storage Mater. 47 (2022) 195–202, http://dx.doi.org/10.1016/j.ensm.2022.02.025.

[18] J. Hu, H. Wang, B. Xiao, P. Liu, T. Huang, Y. Li, X. Ren, Q. Zhang, J. Liu, X. Ouyang, X. Sun, Challenges and approaches of single-crystal Ni-rich layered cathodes in lithium batteries, Natl. Sci. Rev. 10 (12) (2023) 1–20, http://dx.doi.org/10.1093/nsr/nwad252.

[19] Z. Hu, Q. Huang, W. Cai, Z. Zeng, K. Chen, Y. Sun, Q. Kong, W. Feng, K. Wang, Z. Wu, Y. Song, X. Guo, Research progress on enhancing the performance of high nickel single crystal cathode materials for lithium-ion batteries, Ind. Eng. Chem. Res. 62 (6) (2023) 2410–2427, http://dx.doi.org/10.1021/acs.iecr.2c04021.

[20] Y. Bi, J. Tao, Y. Wu, L. Li, Y. Xu, E. Hu, B. Wu, J. Hu, C. Wang, J.-G. Zhang, Y. Qi, J. Xiao, Reversible planar gliding and microcracking in a single-crystalline Ni-rich cathode, Science 370 (6522) (2020) 1313–1317, http://dx.doi.org/10.1126/science.abc3167.

[21] H.-H. Ryu, B. Namkoong, J.-H. Kim, I. Belharouak, C. Yoon, Y.-K. Sun, Capacity fading mechanisms in Ni-rich single-crystal NCM cathodes, ACS Energy Lett. 6 (8) (2021) 2726–2734, http://dx.doi.org/10.1021/acsenergylett.1c01089.

[22] J. Zhu, S. Sharifi-Asl, J. Garcia, H. Iddir, J. Croy, R. Shahbazian-Yassar, G. Chen, Atomic-level understanding of surface reconstruction based on $Li[Ni_xMn_yCo_{1-x-y}]O_2$ single-crystal studies, ACS Appl. Energy Mater. 3 (5) (2020) 4799–4811, http://dx.doi.org/10.1021/acsaem.0c00411.

[23] M. Ge, S. Wi, X. Liu, J. Bai, S. Ehrlich, D. Lu, W.-k. Lee, Z. Chen, F. Wang, Kinetic limitations in single-crystal high-nickel cathodes, Angew. Chem. Int. Ed. 60 (32) (2021) 17350–17355, http://dx.doi.org/10.1002/anie.202012773.

[24] M. Lain, J. Brandon, E. Kendrick, Design strategies for high power vs. High energy lithium ion cells, Batteries 5 (4) (2019) 64, http://dx.doi.org/10.3390/batteries5040064.

[25] Y. Chen, Y. Lakhdar, L. Chen, B. Kishore, J. Choi, E. Williams, D. Spathara, R. Jackowska, E. Kendrick, Accurate voltage prediction for lithium and sodium-ion full-cell development, Next Energy 5 (2024) 100166, http://dx.doi.org/10.1016/j.nxener.2024.100166.

[26] L. Couto, M. Charkhgard, B. Karaman, N. Job, M. Kinnaert, Lithium-ion battery design optimization based on a dimensionless reduced-order electrochemical model, Energy 263 (2023) 125966, http://dx.doi.org/10.1016/j.energy.2022.125966.

[27] M. Duquesnoy, C. Liu, V. Kumar, E. Ayerbe, A. Franco, Toward high-performance energy and power battery cells with machine learning-based optimization of electrode manufacturing, J. Power Sources 590 (2024) 233674, http://dx.doi.org/10.1016/j.jpowsour.2023.233674.

[28] V. Sulzer, S.G. Marquis, R. Timms, M. Robinson, S.J. Chapman, Python battery mathematical modelling (PyBaMM), J. Open Res. Softw. 9 (1) (2021) 14, http://dx.doi.org/10.5334/jors.309.

[29] B. Planden, N.E. Courtier, M. Robinson, A. Khetarpal, F. Brosa Planella, D.A. Howey, PyBOP: A Python package for battery model optimisation and parameterisation, 2024, arXiv:2412.15859.

[30] B.H. Toby, EXPGUI, a graphical user interface for GSAS, J. Appl. Crystallogr. 34 (2) (2001) 210–213, http://dx.doi.org/10.1107/S0021889801002242.

[31] Y. Chen, J. Key, K. O'Regan, T. Song, Y. Han, E. Kendrick, Revealing the rate-limiting electrode of lithium batteries at high rates and mass loadings, Chem. Eng. J. 450 (138275) (2022) 138275, http://dx.doi.org/10.1016/j.cej.2022.138275.

[32] Y. Zhang, J. Bailey, Y. Sun, A. Boyce, W. Dawson, C. Reynolds, Z. Zhang, X. Lu, P. Grant, E. Kendrick, P. Shearing, D. Brett, Applications of advanced metrology for understanding the effects of drying temperature in the lithium-ion battery electrode manufacturing process, J. Mater. Chem. A 10 (19) (2022) 10593–10603, http://dx.doi.org/10.1039/d2ta00861k.

[33] C.-H. Chen, F. Brosa Planella, K. O'Regan, D. Gastol, W. Widanage, E. Kendrick, Development of experimental techniques for parameterization of multi-scale lithium-ion battery models, J. Electrochem. Soc. 167 (8) (2020) 080534, http://dx.doi.org/10.1149/1945-7111/ab9050.

[34] J. Landesfeind, J. Hattendorff, A. Ehrl, W. Wall, H. Gasteiger, Tortuosity determination of battery electrodes and separators by impedance spectroscopy, J. Electrochem. Soc. 163 (7) (2016) A1373–A1387, http://dx.doi.org/10.1149/2.1141607jes.

[35] S. Malifarge, B. Delobel, C. Delacourt, Determination of tortuosity using impedance spectra analysis of symmetric cell, J. Electrochem. Soc. 164 (11) (2017) E3329–E3334, http://dx.doi.org/10.1149/2.0331711jes.

[36] N. Hallemans, N.E. Courtier, C.P. Please, B. Planden, R. Dhoot, R. Timms, S.J. Chapman, D. Howey, S.R. Duncan, Physics-based battery model parametrisation from impedance data, J. Electrochem. Soc. 172 (6) (2025) 060507, http://dx.doi.org/10.1149/1945-7111/add41b.

[37] S. Marquis, V. Sulzer, R. Timms, C. Please, S. Chapman, An asymptotic derivation of a single particle model with electrolyte, J. Electrochem. Soc. 166 (15) (2019) A3693–A3706, http://dx.doi.org/10.1149/2.0341915jes.

[38] S. Xu, K.-H. Chen, N. Dasgupta, J. Siegel, A. Stefanopoulou, Evolution of dead lithium growth in lithium metal batteries: Experimentally validated model of the apparent capacity loss, J. Electrochem. Soc. 166 (14) (2019) A3456–A3463, http://dx.doi.org/10.1149/2.0991914jes.

[39] J. Marshall, D. Gastol, R. Sommerville, B. Middleton, V. Goodship, E. Kendrick, Disassembly of Li ion cells—Characterization and safety considerations of a recycling scheme, Metals 10 (6) (2020) 773, http://dx.doi.org/10.3390/met10060773.

[40] Y. Yamada, Y. Iriyama, T. Abe, Z. Ogumi, Kinetics of lithium ion transfer at the interface between graphite and liquid electrolytes: Effects of solvent and surface film, Langmuir 25 (21) (2009) 12766–12770, http://dx.doi.org/10.1021/la901829v.

[41] Z. Ogumi, Interfacial reactions of lithium-ion batteries, Electrochemistry 78 (5) (2010) 319–324, http://dx.doi.org/10.5796/electrochemistry.78.319.

[42] Y. Li, Y. Qi, Energy landscape of the charge transfer reaction at the complex Li/SEI/electrolyte interface, Energy Env. Sci. 12 (2019) 1286–1295, http://dx.doi.org/10.1039/C8EE03586E.

[43] E. Trevisanello, R. Ruess, G. Conforto, F. Richter, J. Janek, Polycrystalline and single crystalline NCM cathode materials—Quantifying particle cracking, Active Surface Area, and lithium diffusion, Adv. Energy Mater. 11 (18) (2021) http://dx.doi.org/10.1002/aenm.202003400.

[44] K.-E. Kim, J. Jeong, Y. Lee, H. Lim, K. Chung, H. Kim, S.-O. Kim, Enhancing high-voltage structural stability of single-crystalline Ni-rich $LiNi_{0.9}Mn_{0.05}Co_{0.05}O_2$ cathode material by ultrathin Li-rich oxide layer for lithium-ion batteries, J. Power Sources 601 (2024) 234300, http://dx.doi.org/10.1016/j.jpowsour.2024.234300.

[45] X. Liu, Y. Zeng, W. Yuan, G. Zhang, H. Zheng, Z. Chen, Advances in multi-scale design and fabrication processes for thick electrodes in lithium-ion batteries, Energy Rev. 3 (2) (2024) 100066, http://dx.doi.org/10.1016/j.enrev.2023.100066.

[46] K. Gallagher, S. Trask, C. Bauer, T. Woehrle, S. Lux, M. Tschech, P. Lamp, B. Polzin, S. Ha, B. Long, Q. Wu, W. Lu, D. Dees, A. Jansen, Optimizing areal capacities through understanding the limitations of lithium-ion electrodes, J. Electrochem. Soc. 163 (2) (2016) A138–A149, http://dx.doi.org/10.1149/2.0321602jes.

[47] X. Zhang, A. Wang, X. Liu, J. Luo, Dendrites in lithium metal anodes: Suppression, regulation, and elimination, Acc. Chem. Res. 52 (11) (2019) 3223–3232, http://dx.doi.org/10.1021/acs.accounts.9b00437.

[48] J. Landesfeind, H. Gasteiger, Temperature and concentration dependence of the ionic transport properties of lithium-ion battery electrolytes, J. Electrochem. Soc. 166 (14) (2019) A3079–A3097, http://dx.doi.org/10.1149/2.0571912jes.

[49] T.L. Kirk, C.P. Please, S. Jon Chapman, Physical modelling of the slow voltage relaxation phenomenon in lithium-ion batteries, J. Electrochem. Soc. 168 (6) (2021) 060554, http://dx.doi.org/10.1149/1945-7111/ac0bf7.